Brillouin-zone-selection effects in graphite photoelectron angular distributions

Eric L. Shirley and L. J. Terminello
Lawrence Livermore National Laboratory, P.O. Box 808, Livermore, California 94551

A. Santoni
European Synchrotron Radiation Facility, Boîte Postale 220, 38043 Grenoble Cedex, France

F. J. Himpsel
IBM Research Division, Thomas J. Watson Research Center, P.O. Box 218, Yorktown Heights, New York 10598
(Received 1 August 1994)

Experimental and theoretical graphite valence-band photoelectron angular distributions are presented and compared. We observe a zone-selection effect, wherein interference between photoelectron amplitudes from the two atoms in each graphene unit cell cause both σ and π states to appear with different intensity in otherwise equivalent Brillouin zones. To simulate the experimental graphite valence-band photoelectron angular distributions, our simple model includes effects of (1) valence-band wave functions and (2) the relative emission path-length difference, from the atoms in each unit cell to one's detector (which is determined by the experimental geometry).

I. INTRODUCTION

Since the earliest studies of solids by angle-resolved, photoelectron spectroscopy (ARPES),[1] graphite has served as a useful material in demonstrating the efficacy of this technique.[2–6] In principle, photoelectron spectroscopy enables one to probe the wave functions and energies of occupied electron states in a material. Electrons originating from near a surface are observed with the greatest intensity, because of the finite mean free paths of photoelectrons in solids. If one has a periodic, single-crystal sample, with a high-quality, simple surface termination, the energy-dependent, photoelectron angular distribution (PAD) may be used to map the valence-band structure.[6–8]

Photons typically have momenta small compared with Brillouin-zone dimensions. Thus, a photoelectron's vacuum momentum may be related directly to the momentum of the particle's initial state. The momentum of an electron parallel to the surface is preserved during photoemission, modulo surface reciprocal-lattice vectors, due to translational periodicity parallel to the surface. Because of the solid's surface termination, meanwhile, the electron's momentum perpendicular to the surface cannot be a good quantum number. Nonetheless, due to the nearly-free-electron-like dispersion of moderately energetic photoelectrons—say, those excited by photons with energy $h\nu > 50$ eV—a photoelectron's momentum perpendicular to the surface is often restricted to a narrow range of values.

Certain issues concerning an electron's momentum are simplified in graphite, due to the layered structure of this material. In many instances, including the present work, graphite may be treated as an essentially two-dimensional solid. In graphite, the interactions between the graphene sheets of carbon atoms are fairly weak. Consequently, interlayer banding effects lead to band dispersion, in the direction perpendicular to the sheets, on the order of only a few percent of the occupied, valence bandwidth.[9,10] Analyzing a PAD is usually somewhat complicated, for the problem of isoenergetic photoelectrons leaving a solid in various directions, because all three components of the initial-state momentum vary with the direction of exit. Meanwhile, the (practically) two-dimensional quality of the graphite valence bands minimizes the need to identify the initial-state momentum perpendicular to the layers.[1] (The sheets lie parallel to the surface in the graphite we discuss.)

In this work, we present numerically simulated and experimentally determined PAD's for a single-crystal sample of kish graphite provided by Takahashi. This was, however, a multiple-domain sample, but with domain-size smaller than the synchrotron-radiation beam diameter. Therefore, it was effectively a single-crystal, single-domain sample. This is discussed further by Santoni *et al.*,[6] by whom the experimental data, of which some have already been reported in that work, were collected using a display-type electron analyzer with an 84°-full-cone angle of acceptance for photoelectrons. Because data were gathered using monochromatic, incident synchrotron radiation, while collecting electrons at one energy, measured PAD's displayed *constant-energy contours* in the graphite band structure.

To simulate the PAD's, the theoretical model we use includes effects of both band structure and photoexcitation matrix elements. Band structure affects PAD's simply because energy and momentum need to be conserved during photoemission. In general, matrix-element effects involve both the initial- and final-state wave functions. For the graphite valence bands studied here, most of the matrix-element effects are governed by the form of the initial-state wave function. A single-plane-wave description of the final state is sufficient to model the salient features present in the PAD's. We do not include effects

which are realized only in a more complete treatment of the final state, such as photoelectron diffraction. Compared to band structure and the simplest matrix-element effects, phenomena like photoelectron diffraction would lead to a relatively smoother and weaker modulation of intensities found in the range of energies sampled by our PAD's.[11]

In reciprocal space, the band structure of a crystal is periodic, and it is also highly symmetrical about high-symmetry points in the Brillouin zone. This is demonstrated pictorially in the periodic-zone scheme.[12] Therefore, one might look for concomitant periodicity and/or symmetry in PAD's. It is the main goal of this work to explain the conspicuous lack of such periodicity and/or symmetry in contributions, from both the shallowest π and σ states, to measured PAD's.[6] In particular, states observed on one side of a zone boundary, such as in the first Brillouin zone, would be absent, or much weaker, in the next-higher zone,[1,3] and vice versa.

One might refer to the above symmetry breaking as a zone-selection rule. As we discuss below, this effect has been noted before. It is desirable to identify the mechanism leading to such an alleged selection rule. In particular, we want to establish which of two scenarios is true. In the first scenario, a zone-selection effect follows from a strict selection rule, based on rigorous arguments regarding the impact of symmetry on a photoexcitation matrix element. In the second scenario, a zone-selection effect follows merely from a matrix-element effect, not based on rigorous arguments of symmetry. The second scenario may arise when, due to achieving different final states, concomitant variations in a photoexcitation matrix element can lower the symmetry of a PAD from that of the periodic-zone-scheme band structure. In the case of LiF,[7,13] for instance, there were strong variations in photoexcitation matrix elements, particularly between opposite sides of zone boundaries, leading to broken symmetries in PAD's. Nonetheless, the relevant, photoexcitation transition matrix-elements never went completely to zero for reasons of symmetry.

We examine closely the two following, observed zone-selection effects in PAD's from graphite. First, only part of the constant-energy contours of the π bands are seen near the zone corners. Second, the shallowest σ states, which occur at the zone center, are not seen in the first Brillouin zone, but they are seen in higher Brillouin zones. One can explain both of these effects by straightforward application of Fermi's golden rule.[14] We indicate whether the effects are strict selection rules, or only matrix-element effects. Others have noticed the selection effect for the π states in the past.[15,3] Some have indicated that this effect might arise from the discontinuous variation in the π band group velocity near the zone corners.[15] Williams[3] suggested that it might arise from the behavior of the initial-states' momentum distributions. The latter explanation is more precise, although the behavior of the relevant momentum distributions and the group-velocities' behavior are both related to the peculiar dispersion of the graphite π states near zone corners. We have not found the zone-selection effect involving σ states reported elsewhere.

In our experiments, the ability to measure valence-band PAD's as a series of constant-energy contours in reciprocal space revealed the zone-selection effects in graphite most efficaciously. However, this was not the sole motivation for this work. Similar zone-selection effects, found in valence-band PAD's from other materials (e.g., LiF), have also needed to be addressed. It was important in this work, however, that the PAD's were obtained using an 84°-full-cone detector and display-type analyzer,[16] and presented in a fashion exploiting the method of data collection, to pictorially demonstrate the zone-selection effects most plainly.[6] In particular, this method of data presentation helped to reveal the σ-states' zone-selection effect.

We refer the reader to the earlier report by Santoni *et al.*[6] for details of the experiments, whereas this work emphasizes the theoretical explanation of the observed zone-selection effects. First, we discuss relevant aspects of the crystal and electronic structure of graphite. Second, we analyze the photoexcitation matrix elements between the valence, initial states and plane-wave, final states. This involves both the atomic characters of the initial states and the crystal structure. Third, we discuss the zone-selection effects seen for the π states, and we compare theoretical and experimental PAD's as a function of photon and electron energies, presenting the **k**-space intensities in the form of gray-scale images. Fourth, we similarly discuss the zone-selection effects seen for the σ states. Finally, we close with a summary and outlook.

II. CRYSTAL AND ELECTRONIC STRUCTURE OF GRAPHITE

A. Crystal structure

Before discussing the electron states of graphite, we need to discuss the atomic coordinates. We suggest that the zone-selection effects discussed in this work would arise even for a single sheet of graphite (viz. graphene). It is desirable that a description based on a single sheet would be adequate. A physical model would not be as robust, otherwise, if it depended on the multiple-layer aspects of graphite (e.g., the stacking sequence). On the other hand, the model presented here does depend on the orientation of the graphene layers (the orientation with respect to the c axis, and the angle of rotation about that axis). This is only because the direction of an electron's momentum, with respect to a graphene-sheet's angle of rotation, needs to be ascertained. We conduct our discussion almost entirely within a simple, "graphene-sheet picture," although the numerical results presented are based on a single-crystal sample of hexagonal graphite. The numerical results are affected only minimally by interlayer dispersion effects, and we indicate when such effects are important in this work.

Consider a graphene sheet oriented as in Fig. 1(a). There are two carbon atoms per unit cell, labeled "1" and "2". Periodicity of the sheet is indicated by the designated primitive, Bravais-lattice vectors, $\mathbf{a}_1$ and $\mathbf{a}_2$. By combining integer multiples of $\mathbf{a}_1$ and $\mathbf{a}_2$, one forms a gra-

phene sheet's entire set of (two-dimensional) Bravais-lattice vectors $\{\mathbf{R}\}$. The atoms "1" and "2" are at relative positions, within a unit cell, indicated by basis vectors τ_1 and τ_2. We note the following facts about the direct-space lattice, expressed in terms of the bond length, $b \approx 1.42$ Å:

$$\begin{aligned} \mathbf{a}_1 &= \frac{\sqrt{3}}{2} b\hat{\mathbf{x}} + \tfrac{3}{2} b\hat{\mathbf{y}} , \\ \mathbf{a}_2 &= -\frac{\sqrt{3}}{2} b\hat{\mathbf{x}} + \tfrac{3}{2} b\hat{\mathbf{y}} , \\ \tau_2 - \tau_1 &= -\tfrac{1}{3}\mathbf{a}_1 - \tfrac{1}{3}\mathbf{a}_2 . \end{aligned} \tag{1}$$

The reciprocal-space lattice is depicted in Fig. 1(b). (The zone boundaries are shown.) The primitive reciprocal-lattice vectors are given as follows:

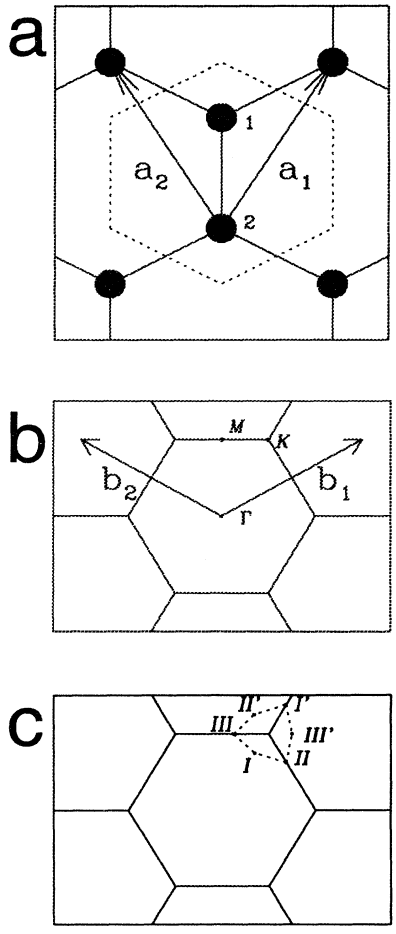

FIG. 1. (a) Unit cell, atomic positions, and primitive lattice vectors for graphene. (b) Reciprocal-space lattice for graphene. Zone boundaries, primitive reciprocal-lattice vectors, and high-symmetry points. The origin is at the center of the panel. (c) Six points on a constant-energy contour around a zone corner, in the π bands. The origin is at the center of the panel.

$$\begin{aligned} \mathbf{b}_1 &= \frac{2\pi}{b}\left[\frac{1}{\sqrt{3}}\hat{\mathbf{x}} + \tfrac{1}{3}\hat{\mathbf{y}}\right] , \\ \mathbf{b}_2 &= \frac{2\pi}{b}\left[-\frac{1}{\sqrt{3}}\hat{\mathbf{x}} + \tfrac{1}{3}\hat{\mathbf{y}}\right] . \end{aligned} \tag{2}$$

Meanwhile, we can specify the crystal momentum $\mathbf{k}$ of an electron through the notation

$$\mathbf{k} = \beta_1 \mathbf{b}_1 + \beta_2 \mathbf{b}_2 . \tag{3}$$

We note the following: at Γ, $\beta_1 = \beta_2 = 0$; at one of the many, equivalent points labeled M, $\beta_1 = \frac{1}{2}$, $\beta_2 = \frac{1}{2}$; at one of the many, equivalent points labeled K, $\beta_1 = \frac{2}{3}$, $\beta_2 = \frac{1}{3}$.

B. Valence electronic structure

In systems with planar, threefold coordinated carbon such as graphite, the carbon-2s- and carbon-2p-derived, occupied, valence states are commonly categorized as σ or π states. The σ states are derived from the 2s and the in-plane 2p orbitals (the $2p_x$ and $2p_y$ in this work). Analogously, the π states are derived from the out-of-plane 2p orbitals (the $2p_z$ here). The unoccupied band states derived from the respective carbon, atomic orbitals are correspondingly referred to as σ^* and π^*. The distinctions between σ and σ^* or between π and π^* are ambiguous in a solid, as compared to in, say acetylene. In the solid, the distinctions should be considered as a distinction between occupied and unoccupied states, though unoccupied states possess a relatively stronger "antibonding" character.

The lowest-energy valence states are the σ states, while the π states overlap the σ ones, and the highest π states lie just below Fermi energy E_F. A large part of σ- and π-state energies are explained partly by the relative strengths of σ and π bonds. Energetically, the lowest π^* states lie just above E_F, and the lowest σ^* states lie slightly higher. The distinction between σ (σ^*) and π (π^*) is valid only for truly planar systems. In graphite, interlayer dispersion effects break the mirror symmetry, of the $\mathbf{k}\cdot\mathbf{p}$ Hamiltonian, necessary for such a distinction. This leads to the admixture of σ and π character in the graphite band states. Stronger σ-π hybridization occurs in fullerene cages[17] and tubules,[18,19] due to the curvatures of the graphene networks present in these systems. We may neglect σ-π hybridization effects in this work.

A reasonable band structure for graphite may be parametrized within an orthogonal, tight-binding framework. We do this using the Slater-Koster method.[20] Different tight-binding parameters are used for the σ and π states. The parameters in the tight-binding Hamiltonian are adjusted to obtain agreement with proper, quasiparticle results for graphite. These results were provided by Zhu and Louie,[9] who found a total, occupied valence bandwidth of 21.5 eV, with the σ states as high as 3.9 eV below E_F, and the occupied, π band being 7.4 eV wide. Our tight-binding band structure is given in Fig. 2, for a graphene sheet. The graphite band structure is similar to the graphene band structure, except for a doubling in number, and slight splitting, of the bands. Further de-

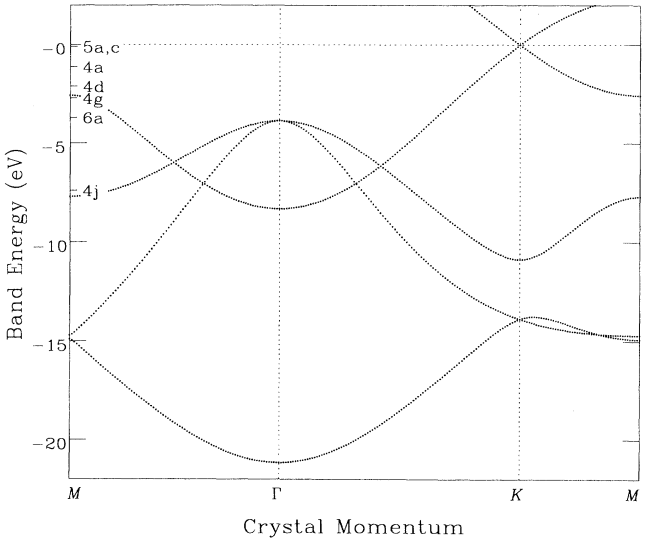

FIG. 2. Band structure for graphene. Band energies measured with respect to the Fermi energy, indicated with a horizontal, dashed line. Energies associated with photoelectron angular distributions in Figs. 4–6 are indicated by labeling of panels displaying experimental data.

tails regarding the tight-binding Hamiltonian are available upon request.[21]

We indicate the eight-electron orbitals in the graphene unit cell–i.e., one "s" and three "p" orbitals, on each of two carbon atoms—by an index, μ: e.g., we specify the "p_y" orbital on atom "2" with $\mu \equiv p_y{:}2$. In a cell at lattice site $\mathbf{R}$, the μth orbital has the form

$$\phi_\mu(\mathbf{r}-\tau_\mu-\mathbf{R}) ,$$

τ_μ being the coordinated of the atom hosting orbital μ. Atomic orbitals are approximated by a separation of variables:

$$\phi_\mu(\mathbf{x}) \approx f_\mu(|\mathbf{x}|) Y_\mu(\hat{\mathbf{x}}) , \tag{4}$$

specifying radial and angular dependences of the atomic orbital. The Y functions are ($l=0$ or 1) angular harmonics. A state in the nth band with crystal momentum $\mathbf{k}$ has energy $\epsilon^{n\mathbf{k}}$, and is given as

$$\Psi^{n\mathbf{k}}(\mathbf{r}) = \frac{1}{\sqrt{N}} \sum_{\mathbf{R}} e^{i\mathbf{k}\cdot\mathbf{R}} \sum_{\mu} C_\mu^{n\mathbf{k}} \phi_\mu(\mathbf{r}-\tau_\mu-\mathbf{R}) . \tag{5}$$

There is a normalization factor, due to there being N unit cells in the crystal; we work in the $N \to \infty$ limit.

In this work, we discuss two kinds of states. We describe these states now, but why these particular states are of interest will be illustrated later. To enhance our discussion, the orbitals are depicted in Fig. 3. The first states are the highest σ states, which are located at zone center. These states are doubly degenerate, and these states can be given by

$$C^{3\Gamma}_{p_x:1} = -C^{3\Gamma}_{p_x:2} = 1/\sqrt{2} ,$$

or

$$C^{4\Gamma}_{p_y:1} = -C^{4\Gamma}_{p_y:2} = 1/\sqrt{2} ,$$

with the remaining C's being zero.

The π states near the zone corners are more interesting and slightly more complicated than the above σ states. The unusual behavior of these π bands near the zone corners leads to (1) the semimetallic properties of graphite (whose Fermi surface would have precisely zero area, were it not for interlayer, banding effects);[10] (2) the rapid variations in the band group velocities near the zone corners; (3) a symmetry-breaking effect in scanning-tunneling-microscopy images of high-quality, single-

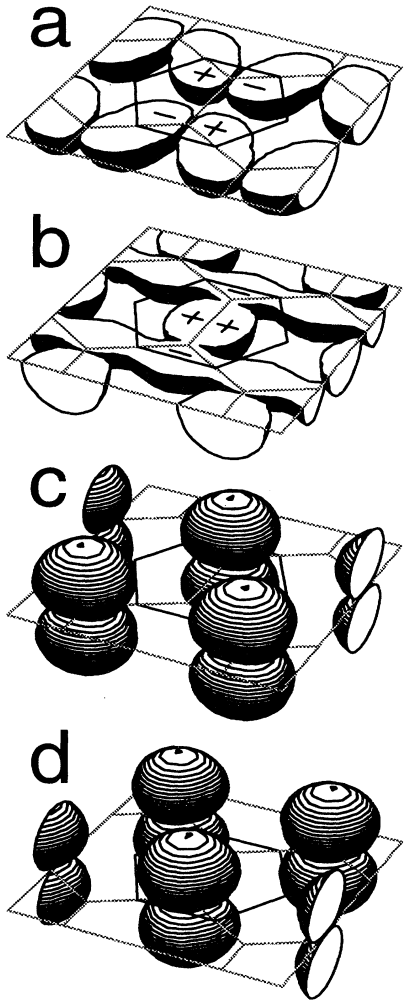

FIG. 3. Regions of high probability density for the highest σ states (a) and (b), and for the π states, in graphene (c) and (d). Regions drawn as solid volumes within which probability density exceeds a certain value. Bonds between carbon atoms, and a bounding box to guide the eye, in gray. Unit-cell boundaries are indicated in black. In parts (a) and (b), probability densities are shown only beneath the sheet, for the sake of presentation; the sign of the wave function is indicated. Parts a and b each correspond to a σ state. In parts (c) and (d), the π orbitals on each of two atoms are indicated. Linear combination of these, using complex coefficients, form the π states.

crystal graphite (which depends on interlayer banding effects);[22] and (4) some of the zone-selection effects which we are discussing.

Although our tight-binding Hamiltonian includes banding effects beyond nearest-neighbor interactions, the results we obtain for π states near the zone corners can be illustrated within a nearest-neighbor-only, tight-binding picture. We, therefore, conduct our discussion regarding the π states within this simpler framework. The system of π and π^* states may be thought of as a set of two-level systems, with a different two-level Hamiltonian to be solved at each value of $\mathbf{k}$. The π and π^* states are described at each $\mathbf{k}$ by the following secular equations:

$$\begin{aligned} H_{p_z:1,p_z:1}(\mathbf{k})C^{n\mathbf{k}}_{p_z:1}+H_{p_z:1,p_z:2}(\mathbf{k})C^{n\mathbf{k}}_{p_z:2}=\epsilon^{n\mathbf{k}}C^{n\mathbf{k}}_{p_z:1}\ , \\ H_{p_z:2,p_z:1}(\mathbf{k})C^{n\mathbf{k}}_{p_z:1}+H_{p_z:2,p_z:2}(\mathbf{k})C^{n\mathbf{k}}_{p_z:2}=\epsilon^{n\mathbf{k}}C^{n\mathbf{k}}_{p_z:2}\ . \end{aligned} \tag{6}$$

All other C's are zero. We leave the index n unspecified, because the π and π^* bands cross σ and σ^* bands, in addition to other bands, as one goes through the Brillouin zone. In the nearest-neighbor-only, tight-binding picture, we have $H_{p_z:1,p_z:1}=H_{p_z:2,p_z:2}=\epsilon^0_\pi$, a term energy. There is also a π-π transfer amplitude t. We note that t is negative. For the off-diagonal parts of the Hamiltonian, we have

$$\begin{aligned} H_{p_z:1,p_z:2}(\mathbf{k})&=H^*_{p_z:2,p_z:1}(\mathbf{k}) \\ &=t\,[1+\exp(2\pi i\beta_1)+\exp(2\pi i\beta_2)]\ , \end{aligned} \tag{7}$$

where β_1 and β_2 are specified by $\mathbf{k}$. The π^* and π energies are given as $\epsilon^0_\pi\pm|H_{p_z:1,p_z:2}(\mathbf{k})|$. The moduli of the two relevant C's are both $1/\sqrt{2}$, and the relative phase between the two C's for the π state is given as follows:

$$\frac{C^{n\mathbf{k}}_{p_z:1}}{C^{n\mathbf{k}}_{p_z:2}}=-\frac{H_{p_z:1,p_z:2}(\mathbf{k})}{|H_{p_z:1,p_z:2}(\mathbf{k})|}\ . \tag{8}$$

We note that the two-level Hamiltonian in Eq. (6) would be degenerate without the off-diagonal parts, and these off-diagonal parts are zero at the zone corners. By following a path around any zone corner, one would observe that the off-diagonal parts exhibit all complex phases. Therefore, the relative phase between $C^{n\mathbf{k}}_{p_z:1}$ and $C^{n\mathbf{k}}_{p_z:2}$—the only two nonzero C coefficients—varies correspondingly as one moves around the zone corners [see Fig. 1(c)].

III. PHOTOEXCITATION, PLANE-WAVE MATRIX ELEMENTS

One may write a dipole-approximation expression for a photoexcitation matrix element,

$$M^{n\mathbf{k}}\propto\int d^3r e^{-i\mathbf{k}\cdot\mathbf{r}}(\mathbf{p}\cdot\mathbf{A})\Psi^{n\mathbf{k}}(\mathbf{r})\ . \tag{9}$$

The matrix element is given above as a function of the total $\mathbf{k}$ of the assumed, plane-wave, final state. We, therefore, specify the initial state $\mathbf{k}$ in a periodic-zone scheme, exploiting the periodicity of the band states and band energies in reciprocal space.

Within the tight-binding framework used in this work, one may rewrite Eq. (9) more explicitly:

$$M^{n\mathbf{k}}\propto(\mathbf{k}\cdot\hat{\boldsymbol{\lambda}})\sum_\mu C^{n\mathbf{k}}_\mu e^{-i\mathbf{k}\cdot\tau_\mu}\tilde{f}_\mu(|\mathbf{k}|)Y_\mu(\hat{\mathbf{k}})\ . \tag{10}$$

In this relation, there is a missing proportionality constant, which is however independent of the initial state. On the right-hand side, the first factor acts to select the direction of outgoing photoelectrons, based on the polarization vector of the incident radiation $\hat{\boldsymbol{\lambda}}$. This leads to angular anisotropy (i.e., absence of the crystal-surface symmetry) in PAD's. Next, the summation over atomic orbitals can lead to interesting interference effects for two reasons. First, it follows because of variation in the relative phases of the C's in the electron initial-state wave function. Second, there generally are different path lengths from the various atoms in each unit cell to one's detector, which leads to the τ_μ-dependent structure factors. In this work, the two-dimensional character of graphite implies that these structure factors will affect the PAD's chiefly due to the momentum *parallel* to the graphene sheets. The $\tilde{f}$ functions are appropriate Fourier transforms of the f functions. We have evaluated them using results of self-consistent-field, Hartree-Fock atom calculations.[23] However, the $\tilde{f}$ functions are unimportant in this work, since they only provide overall, angle-independent prefactors to the PAD's. On the other hand, the Y functions influence the PAD's in a very important way, through angle-dependent factors.

In the theoretical PAD's, we use the following expression for the electron flux for a momentum $\mathbf{k}$:

$$I(\mathbf{k})=A\,2\pi\sum_n\delta(\epsilon^{n\mathbf{k}}+h\nu-\hbar k^2/2m)|M^{n\mathbf{k}}|^2\ . \tag{11}$$

A is an unspecified, but constant, prefactor. In our calculations, the δ function was Lorentz broadened to simulate an experimental measurement condition with an energy, band-pass filter having a 0.5-eV full width at half maximum.

We remind the reader that we are not including photoelectron-diffraction effects, since we do not consider effects of atomic scattering centers on the outgoing, plane-wave, final state. In another material, LiF, we have found that PAD's are affected more strongly by such effects.[13] We anticipate that photoelectron diffraction does not strongly influence the zone-selection phenomena found here. Instead, including photoelectron-diffraction effects in our model would introduce a smooth and weakly varied envelope modulating the theoretical PAD's.

IV. ZONE-SELECTION EFFECTS

For all of the measurements, neither symmetrization nor noise-filtering procedures have been applied to the data presented. For clarity in presentation, however, the data were clipped to suppress areas corresponding to experimentally inaccessible phase space and/or spurious signal near the edges of the field of view. Further, contrast was uniformly adjusted so as to render background noise essentially invisible. There is also nonideality of the images, resulting from uncompensated angular distor-

tions by the detector. Despite such perturbations from ideality in the PAD's, all relevant features in the experimental data are plainly visible.

With the experimental constraint of a fixed 84°-full-cone angular acceptance, photoelectrons of a given kinetic energy can be probed from only a particular region of reciprocal space. The best momentum resolution is found at low kinetic energies, which follows from an energy-independent angular resolution. Working at higher kinetic energies (using higher-energy photons) permits the study of larger regions of reciprocal space, though at the cost of poorer momentum resolution.

We discuss two particular zone-selection effects in detail. Several others are discussed only briefly, in passing.

A. π states

For electron states on a constant-energy contour near a zone corner, contributions to the PAD's from the π states will vary as a factor which changes smoothly, times a factor of the form

$$|\zeta(\beta_1,\beta_2)|^2=\left|1+e^{[2\pi i(\beta_1+\beta_2)]/3}\left[\frac{1+e^{-2\pi i\beta_1}+e^{-2\pi i\beta_2}}{|1+e^{-2\pi i\beta_1}+e^{-2\pi i\beta_2}|}\right]\right|^2.$$

This follows from Eqs. (7), (8), and (10). All that influences the above factor is the relative phase between $C^{n\mathbf{k}}_{p_z:1}$ and $C^{n\mathbf{k}}_{p_z:2}$, and the relative path-length difference from atoms "1" and "2" in each unit cell [cf. Fig. 1(a)] to one's detector. Variations in ζ are, therefore, due to simple interference between two photoelectron wave amplitudes.

We note that ζ changes rapidly near a zone corner. In Table I, we present results for the above expression at six points near one of zone corners, i.e., the corner specified by $\beta_1=\frac{2}{3}$, $\beta_2=\frac{1}{3}$. These six points are illustrated in Fig. 1(c). Due to the variations in $|\zeta(\beta_1,\beta_2)|^2$, we find that only part of the contours are visible in PAD's. Experimental results are shown adjacent to the theoretical results in Fig. 4. The photon energy used in the experiments was $\approx$50 eV. Each energy slice shown in Fig. 4 measures states at the indicated energy with respect to E_F. Over all, we see that our model for zone selection in π-state emission is substantiated by the experimental results shown in Fig. 4. The interference effects are in agreement between theory and experiment.

We note that both the relative phase between the C coefficients and path-length effects [cf. Eq. (10)] are needed to explain the data. Whereas the present, tight-binding model finds zero intensity from the π states in the second Brillouin zone (along the $\bar{K}$-$\bar{M}$-$\bar{K}$ line, going away from the first Brillouin-zone's center), these π states may have nonzero (though small) intensity in experiment. The intensity is at most very small, however, based on the experimental data. This intensity may be nonzero because of trigonal distortions of the nominally p_z orbitals in real graphite. Such distortions (through admixture of higher-angular-momentum orbitals into the nominally p_z orbitals) are not considered in the present, tight-binding framework.

The results of Figs. 4(j)–4(l) are perhaps the only results showing significant effects related to the third dimension. In theory [cf. Fig. 4(l)], a PAD could include two sixfold symmetric, fluted contours and two nearly circular contours in the first zone.[24] [One of the fluted contours lies right on top of a circular contour in Fig. 4(l)]. The fluted contours are due to σ states, and these are discussed in the next subsection. The circular contours are due to π states. Only one circular contour is seen in the theoretical PAD. Near the zone center, the coefficients of all of the p_z orbitals *within* each graphene sheet have nearly the same phase. In *AB*-stacked, hexagonal graphite, however, there are two π-bands split in energy (by up to about 1 eV), and there is a difference between the band states regarding the relative phases of the above coefficients *between* sheets. Depending on the interlayer spacing times photoelectron momentum perpendicular to the sheets, destructive and constructive interference will occur for emission from one of these π bands and the other, respectively. This is why only one circular contour is visible in Fig. 4(k). The π bands are extremal near the zone center, their energies varying in a parabolic fashion with the distance of $k_\parallel$ from the center. Meanwhile, the bands vary in value by around 1 eV in the $k_\perp$ direction. Hence, even a small uncertainty in momentum perpendicular to the layers—i.e., normal to the surface, in this work—can lead to substantial smearing effects in the $k_\parallel$ directions in isoenergy PAD's. This is perhaps why the experimental PAD [cf. Fig. 4(j)] in the first zone appears as a solid disk instead of two rings. This effect could suppress the ability to resolve the two π bands separately near the zone center, despite an experimental energy pass set to 0.5 eV full width at half maximum.

We also measured the PAD's from the σ and π states

TABLE I. Ratio $C^{n\mathbf{k}}_{p_z:2}/C^{n\mathbf{k}}_{p_x:1}$, relative amplitude of transition matrix element, $\zeta(\beta_1,\beta_2)$, and relative photoelectron intensities for the six points in the Brillouin zone indicated in Fig. 1(c).

Zone point	$C^{n\mathbf{k}}_{p_z:2}/C^{n\mathbf{k}}_{p_z:1}$	$\zeta(\beta_1,\beta_2)$ (arb.)	$\lvert\zeta(\beta_1,\beta_2)\rvert^2$ (arb.)
I	$\exp(-2\pi i/3)$	2	4
II	$\exp(-\pi i/3)$	$\sqrt{3}\exp(\pi i/6)$	3
III	-1	$\sqrt{3}\exp(-\pi i/6)$	3
I'	$-\exp(-2\pi i/3)$	0	0
II'	$-\exp(-\pi i/3)$	$\exp(-\pi i/3)$	1
III'	1	$\exp(\pi i/3)$	1

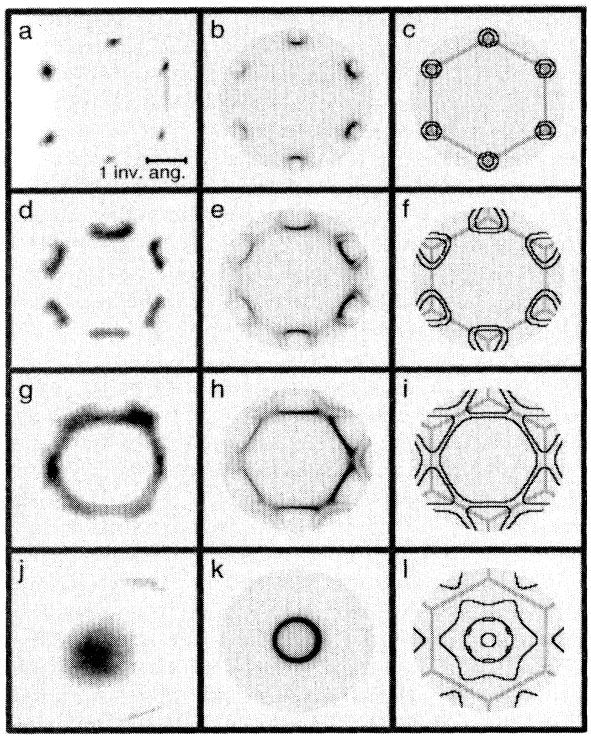

FIG. 4. (a) Experimental photoelectron angular distribution as a function of initial-state momentum parallel to the surface, for states at -1.1 eV with respect to the Fermi energy. Areas of higher flux are darker. The momentum/wave-number scale is indicated. (b) Simulated photoelectron angular distribution obtained using the model described in this paper, the same energy, and the same momentum scale. (c) Theoretical, constant-energy contours in the band structure, the same energy, and the same momentum scale. Panels (d)–(f), same as (a)–(c), but -2.1 eV with respect to Fermi energy. Panels (g)–(i), same as (a)–(c), but -2.8 eV with respect to Fermi energy. Panels (j)–(l), same as (a)–(c), but -7.7 eV with respect to Fermi energy. All panels have a photon energy of ≈ 50 eV.

of graphite at higher kinetic energies, in order to access the second and third Brillouin zones. In Fig. 5, we show theoretical and experimental results for π states at higher photon energies, approximately 150 and 250 eV. The periodicity of electron band states in reciprocal space is seen in the images, but the zone-selection effects just discussed imply that different points on a constant-energy contour are seen with different intensities. This is very clear in the theoretical images, though difficult to see with the limited angular resolution in the experimental images. This effect is also manifested, nonetheless, through different apparent lengths of equal-length zone boundaries. For instance, one may compare the distances between spots near corners of the first Brillouin zone with distances between spots near the ends of the $\bar{K}$-$\bar{M}$-$\bar{K}$ line in the higher zone, going away from the first Brillouin-zone center.

B. σ states

We refer the reader now to the σ states lying 3.7 eV below E_F at the zone center (cf. Fig. 6). The photon energy used in the experiments was ≈ 150 eV. We note that the quasiparticle results by Zhu and Louie predicted this 3.7 eV very well. States at the top of the σ band are not seen in the first Brillouin zone (i.e., at normal emission). However, these states are seen in the neighboring zones. There are two mechanisms responsible for this effect. Each mechanism would suppress normal emission from these highest σ states, and neither mechanism would suppress their emission in other directions.

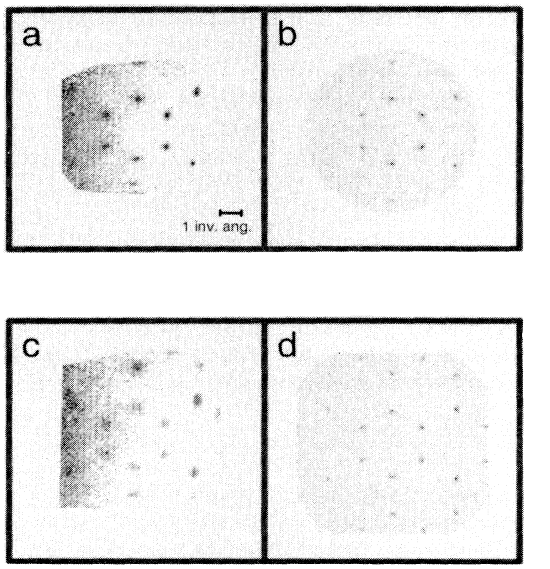

FIG. 5. (a) Experimental photoelectron angular distribution, as a function of initial-state momentum parallel to the surface, for occupied states near the Fermi energy. Zone corners near the areas with higher flux are drawn darker. There is background noise towards the left side of the panel. Photon energy ≈ 150 eV. The momentum/wave-number scale is indicated. (b) Simulated photoelectron angular distribution obtained using the model described in this paper, the same energy, and the same momentum scale. Panels (c)–(d), same as (a)–(b), but with a photon energy of ≈ 250 eV.

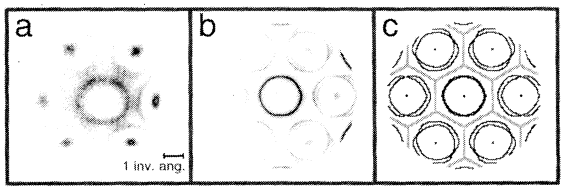

FIG. 6. (a) Experimental photoelectron angular distribution as a function of initial-state momentum parallel to the surface, for states at -3.7 eV with respect to the Fermi energy. Areas of higher flux are darker. The momentum/wave-number scale is indicated. (b) Simulated photoelectron angular distribution obtained using the model described in this paper, the same energy, and the same momentum scale. (c) Theoretical, constant-energy contours in the band structure, the same energy, and the same momentum scale. The points at the zone centers are not part of the same constant-energy contour, but are drawn for reference. The states seen near the higher zone centers lie slightly lower in theory, but are visible due to the finite-energy-resolution effects. Photon energy of ≈ 150 eV.

(1) There is an angular factor, due to the symmetry of the p_x and p_y orbitals, entering via the Y factors in the photoexcitation matrix elements, cf. Eq. (10). This factor goes precisely to zero at normal emission, for both of the σ states.

(2) Even without the above, Y-factor effect, the opposite signs of the two nonzero C coefficients in these σ states imply an exact cancellation of the amplitudes, from the two atoms in each unit cell, in detected photoelectron waves at normal emission. Hence, what we are discussing now is a true selection-rule effect. At normal emission, there is no difference in the path lengths from each of the atoms in each unit cell to one's detector. In the higher Brillouin zones, on the other hand, there is a nonzero difference in these path lengths, so complete destructive interference between waves from the two atoms does not occur. Without taking this path-length difference into account, one would still predict destructive interference in higher zones.

Meanwhile, in the results shown in Fig. 6, one can also see π states. Unlike the σ states, these π states are visible near the center of the first Brillouin zone. For the π states, the C coefficients of the two p_z orbitals have the same sign near the zone center, and the π states have a Y factor favorable for normal emission. On the other hand, the π states are seen more weakly in the second Brillouin zone, but are seen strongly again even further from normal emission—all describable through modulation of a path-length difference. Interference effects work oppositely for the σ and π states. Finally, we note that there is a signal from σ bands seen in Fig. 4(j), in the higher zones, whereas the σ states are not seen at normal emission. This occurs for an analogous reason as in Fig. 6.

V. SUMMARY AND CONCLUSIONS

Historically, graphite has been particularly useful in understanding the principles of ARPES, because of its simple, layered structure. In this work, we have carried out a study of the factors governing intensity variations observed in valence-band photoelectron angular distributions (PAD's) from graphite. We present both theoretical and experimental PAD's from single-crystal graphite. Besides energy- and momentum-conservation constraints, the PAD's from graphite are strongly influenced by photoexcitation matrix-element effects. These involve the symmetries of the atomic orbitals constituting valence-band states, the relative phases of the coefficients of like atomic orbitals on different atoms in each crystal unit cell, and the relative path lengths from various atoms in each unit cell to one's detector.

Brillouin-zone selection effects have been seen in two ways: only some of the states near the top of the π band were detected in PAD's, and there was no signal from the tops of the σ bands in the first Brillouin zone (i.e., at normal emission). Both of these effects were explained by using Fermi's Golden Rule within a simple tight-binding approach. To demonstrate the model used to simulate PAD's, we have presented gray-scale images of theoretical and experimental PAD's. This was done in a fashion appropriate for contemporary display-type analyzers. The photoelectron intensity as a function of emission angle was the quantity represented in the images.

It is interesting to consider the interplay between band-dispersion effects and the present treatment of matrix-elements carried out to simulate the graphite PAD's, on the one hand, and photoelectron-diffraction effects, which are neglected here, on the other hand. It appears that all salient features of graphite PAD's were predicted within the present treatment. This was not true in an analogous study of a more complex material, where valence-band photoelectron-diffraction effects proved to be more critical.[13]

It is gratifying that such striking experimental effects in the valence-band photoelectron angular distributions have been explained using such simple theory. The experimental results constitute an elegant demonstration of the workings of quantum mechanics. Collectively, the Brillouin-zone effects discussed in this work constitute a single, more general interference effect. For the Brillouin-zone selection effects to be properly understood, photoexcitation must be considered as a coherent process, which simultaneously involves the initial- and final-states wave functions on several different atoms. In terms of the formulation set forth in this work, the integral over space which involves these wave functions, used to obtain a photoexcitation matrix element [Eq. (9)], must be carried out prior to squaring the result to obtain a transition rate—the classic "summing before squaring" argument familiar in quantum mechanics.

The results of this work can encourage one to employ suitably adapted theoretical tools to model the electronic structure of other materials through analysis of their valence-band photoelectron angular distributions. Furthermore, similar analysis could be carried out for inverse-photoemission experiments. It might be worthwhile, for instance, to examine inverse PAD's for π^* states near the zone corners in graphite. We predict that exactly the opposite zone-selection rule would be observed from that seen in direct photoemission of graphite. Analysis of inverse-photoemission spectra, collected for electrons at normal incidence, may also provide valuable information regarding the symmetry and ordering of conduction bands in graphite, higher than the first few which are known.

ACKNOWLEDGMENTS

This work was conducted under the auspices of the U.S. Department of Energy, Office of Basic Energy Sciences, Division of Materials Science, by the Lawrence Livermore National Laboratory under Contract No. W-7405-ENG-48. The measurements were conducted at the National Synchrotron Light Source, Brookhaven National Laboratory, which is supported by the U.S. Department of Energy, Division of Materials Sciences and Division of Chemical Sciences. The single-crystal graphite sample, described in Ref. 6, was kindly provided by T. Takahashi, Tohoku University. We are grateful to X. Zhu and S. G. Louie for permitting our use of their quasiparticle results for graphite prior to publication. The tight-binding calculations were carried out using a modified, and extended, program written originally by X. Blase and L. X. Benedict. We benefited from discussions with J. N. Glosli and L. H. Yang.

[1]For a review, see F. J. Himpsel, Adv. Phys. **32**, 1 (1983).
[2]R. F. Willis, B. Feuerbacher, and B. Fitton, Phys. Rev. B **4**, 2441 (1971).
[3]P. M. Williams, Nuovo Cimento **38B**, 216 (1977).
[4]I. T. McGovern, W. Eberhardt, E. W. Plummer, and J. E. Fischer, Physica **99B**, 415 (1980).
[5]T. Takashashi, H. Tokailin, and T. Sagawa, Solid State Commun. **52**, 765 (1984).
[6]A. Santoni, L. J. Terminello, F. J. Himpsel, and T. Takahashi, Appl. Phys. A **52**, 299 (1991).
[7]D. A. Lapiano-Smith, E. A. Eklund, F. J. Himpsel, and L. J. Terminello, Appl. Phys. Lett. **59**, 2174 (1991); F. J. Himpsel, L. J. Terminello, D. A. Lapiano-Smith, E. A. Eklund, and J. J. Barton, Phys. Rev. Lett. **68**, 3611 (1992).
[8]L. J. Terminello, J. A. Carlisle, J. E. Klepeis, C. Mailhiot, F. J. Himpsel, J. J. Barton, and A. Santoni, Bull. Am. Phys. Soc. **39**, 201 (1994).
[9]X. Zhu and S. G. Louie (private communication).
[10]J. C. Charlier, X. Gonze, and J. P. Michenaud, Phys. Rev. B **43**, 4579 (1991); J. C. Charlier, J. P. Michenaud, and X. Gonze, *ibid.* **46**, 4531 (1992).
[11]Two recent reviews on related effects are C. S. Fadley, in *Applications of Synchrotron Radiation Techniques of Materials Science,* edited by D. L. Perry, N. Shinn, R. Stockbauer, K. D'Amico, and L. Terminello, MRS Symposia Proceedings No. 307 (Materials Research Society, Pittsburgh, 1993), p. 261; and C. S. Fadley, in *Synchrotron Radiation Research: Advances in Surface and Interface Science,* edited by Robert Z. Bachrach (Plenum, New York, 1992), Vol. 1, p. 421.
[12]C. Kittel, *Introduction to Solid State Physics,* 6th ed. (Wiley, New York, 1986), p. 222.
[13]E. L. Shirley, L. J. Terminello, J. E. Klepeis, and F. J. Himpsel (unpublished).
[14]K. Gottfried, *Quantum Mechanics* (Benjamin/Cummings, Reading, MA, 1966), Vol. I, p. 443ff.
[15]See, for example, the discussion in Ref. 1.
[16]D. E. Eastman, J. J. Donelon, N. C. Hien, and F. J. Himpsel, Nucl. Instrum. Methods **172**, 327 (1980).
[17]N. Troullier and J. L. Martins, Phys. Rev. B **46**, 1754 (1992).
[18]N. Hamada, S. Sawada, and A. Oshiyama, Phys. Rev. Lett. **68**, 1579 (1992).
[19]X. Blase, L. X. Benedict, E. L. Shirley, and S. G. Louie, Phys. Rev. Lett. **72**, 1878 (1994).
[20]J. C. Slater and G. F. Koster, Phys. Rev. **94**, 1498 (1954).
[21]E. L. Shirley (unpublished).
[22]D. Tománek, S. G. Louie, H. J. Mamin, D. W. Abraham, R. E. Thomson, E. Ganz, and J. Clarke, Phys. Rev. B **35**, 7790 (1987); D. Tománek and S. G. Louie, *ibid.* **37**, 8327 (1988).
[23]E. L. Shirley, Ph.D. thesis, University of Illinois, 1991.
[24]In principle, the *AB* stacking would reduce such sixfold symmetry to threefold in all PAD's. However, incomplete coverage by the top layer of that below it could lead to equal amounts of *A* and *B* termination in one's sample. Meanwhile, our model does not contain the necessary details to distinguish between *A* and *B* termination of a crystal, and our salient results are correspondingly insensitive to any related effects.

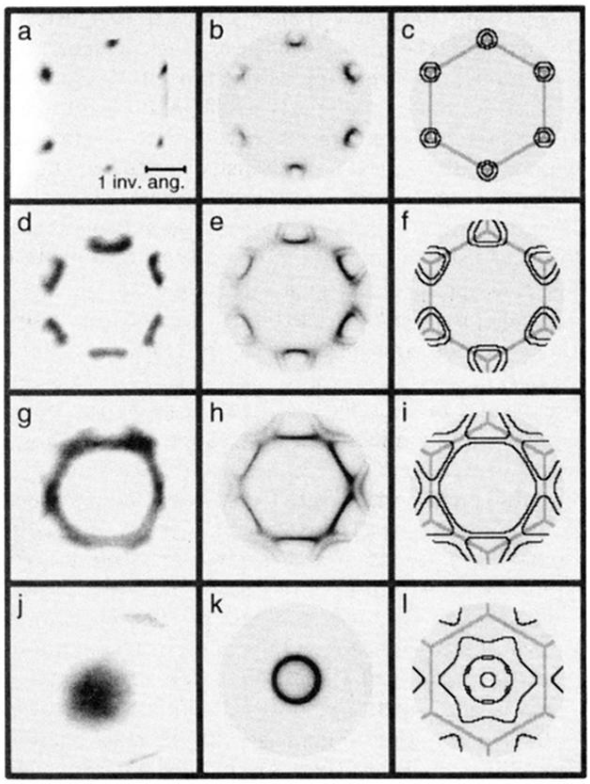

FIG. 4. (a) Experimental photoelectron angular distribution as a function of initial-state momentum parallel to the surface, for states at −1.1 eV with respect to the Fermi energy. Areas of higher flux are darker. The momentum/wave-number scale is indicated. (b) Simulated photoelectron angular distribution obtained using the model described in this paper, the same energy, and the same momentum scale. (c) Theoretical, constant-energy contours in the band structure, the same energy, and the same momentum scale. Panels (d)–(f), same as (a)–(c), but −2.1 eV with respect to Fermi energy. Panels (g)–(i), same as (a)–(c), but −2.8 eV with respect to Fermi energy. Panels (j)–(l), same as (a)–(c), but −7.7 eV with respect to Fermi energy. All panels have a photon energy of ≈ 50 eV.

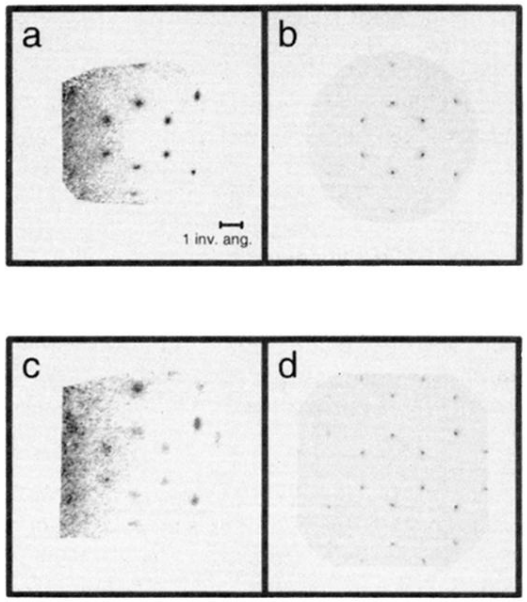

FIG. 5. (a) Experimental photoelectron angular distribution, as a function of initial-state momentum parallel to the surface, for occupied states near the Fermi energy. Zone corners near the areas with higher flux are drawn darker. There is background noise towards the left side of the panel. Photon energy ≈ 150 eV. The momentum/wave-number scale is indicated. (b) Simulated photoelectron angular distribution obtained using the model described in this paper, the same energy, and the same momentum scale. Panels (c)–(d), same as (a)–(b), but with a photon energy of ≈ 250 eV.

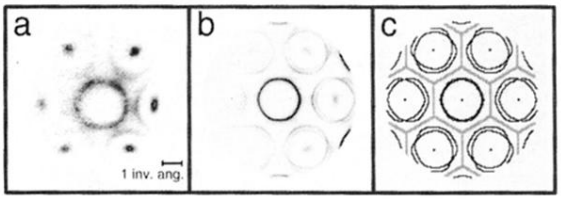

FIG. 6. (a) Experimental photoelectron angular distribution as a function of initial-state momentum parallel to the surface, for states at -3.7 eV with respect to the Fermi energy. Areas of higher flux are darker. The momentum/wave-number scale is indicated. (b) Simulated photoelectron angular distribution obtained using the model described in this paper, the same energy, and the same momentum scale. (c) Theoretical, constant-energy contours in the band structure, the same energy, and the same momentum scale. The points at the zone centers are not part of the same constant-energy contour, but are drawn for reference. The states seen near the higher zone centers lie slightly lower in theory, but are visible due to the finite-energy-resolution effects. Photon energy of ≈ 150 eV.